

Fast Molecular-Dynamics Simulation for Ferroelectric Thin-Film Capacitors Using a First-Principles Effective Hamiltonian

Takeshi Nishimatsu^{1,2}, Umesh V. Waghmare³, Yoshiyuki Kawazoe², and David Vanderbilt¹

¹*Department of Physics and Astronomy, Rutgers University,
136 Frelinghuysen Road, Piscataway, NJ 08544-8019*

²*Institute for Materials Research (IMR), Tohoku University, Sendai 980-8577, Japan*

³*Theoretical Sciences Unit, Jawaharlal Nehru Centre for Advanced
Scientific Research (JNCASR), Jakkur, Bangalore, 560 064, India*

A newly developed fast molecular-dynamics method is applied to BaTiO₃ ferroelectric thin-film capacitors with short-circuited electrodes or under applied voltage. The molecular-dynamics simulations based on a first-principles effective Hamiltonian clarify that dead layers (or passive layers) between ferroelectrics and electrodes markedly affect the properties of capacitors, and predict that the system is unable to hop between a uniformly polarized ferroelectric structure and a striped ferroelectric domain structure at low temperatures. Simulations of hysteresis loops of thin-film capacitors are also performed, and their dependence on film thickness, epitaxial constraints, and electrodes are discussed.

PACS numbers: 77.80.Dj, 77.80.Fm, 64.70.Nd

I. INTRODUCTION

Ferroelectric thin films are beginning to see wide-ranging applications, for example in multilayer capacitors, nonvolatile FeRAMs,¹ and nanoactuators. There is strong pressure to reduce the sizes of such thin-film structures. In recent years, the preparation of oxide thin films by low-temperature non-equilibrium techniques such as molecular beam epitaxy and pulsed-laser deposition have attracted a great deal of attention, as they enable finely controlled growth of epitaxial thin films.²

It is well known that the properties of ferroelectric capacitors are highly influenced by the properties of the interface between the ferroelectrics and the electrodes. For example, the fatigue of ferroelectric capacitors is associated with the appearance of dead layers (or passive layers) near the electrodes,^{3,4,5,6} and imperfect electrodes cannot fully screen the polarization of ferroelectrics,^{7,8} leading to a finite depolarization field in the ferroelectric film. However, the nanosize effects and temperature dependences of ferroelectric capacitor hysteresis, polarization switching, and dynamics of domain wall motion remain poorly known. Experimentally, *in situ* observations are difficult. Theoretically, the long-range Coulomb interaction limits the size and time of molecular-dynamics (MD) simulations, and it has been unclear how to include surface effects and depolarization fields caused by interface structures.

In 1994, King-Smith and Vanderbilt studied the total-energy surface for zone-center distortions of perovskite-type ferroelectric oxides ABO_3 (A is a monovalent or divalent cation and B is a penta- or tetravalent metal) at zero temperature using first-principles calculations with ultrasoft-pseudopotentials and a plane-wave basis set.⁹ Starting from the full symmetric cubic perovskite structure, they define the displacements v_α^τ of atoms τ ($=A, B, O_I, O_{II}, O_{III}$) in the Cartesian directions α ($=x, y, z$) along the Γ_{15} soft-mode normalized direction vectors ξ_α

as

$$\mathbf{v}_\alpha = \begin{pmatrix} v_\alpha^A \\ v_\alpha^B \\ v_\alpha^{O_I} \\ v_\alpha^{O_{II}} \\ v_\alpha^{O_{III}} \end{pmatrix} = u_\alpha \boldsymbol{\xi}_\alpha = u_\alpha \begin{pmatrix} \xi_\alpha^A \\ \xi_\alpha^B \\ \xi_\alpha^{O_I} \\ \xi_\alpha^{O_{II}} \\ \xi_\alpha^{O_{III}} \end{pmatrix}, \quad (1)$$

with the scalar soft-mode amplitude u_α . Under the condition that the strain components η_i ($i = 1, \dots, 6$; Voigt notation; $\eta_1 = e_{11}$, $\eta_4 = e_{23}$) minimize the total energy for each $\mathbf{u} = (u_x, u_y, u_z)$, they expressed the total energy as

$$E^{\text{tot}} = E^0 + \kappa u^2 + \alpha' u^4 + \gamma' (u_x^2 u_y^2 + u_y^2 u_z^2 + u_z^2 u_x^2), \quad (2)$$

where $u^2 = u_x^2 + u_y^2 + u_z^2$, E^0 is the total energy for the cubic structure, κ is half the eigenvalue of the soft mode, and α' and γ' are the constants determined from coupling constants between atomic displacements and strains. Their expression properly describes the coupling of polar atomic-displacement and strain degrees of freedom.

In 1994-1997, Zhong, Vanderbilt, and Rabe^{10,11} and Waghmare and Rabe¹² expanded Eq. (2) from a mean-field framework to a local-mode framework, replacing \mathbf{u} by $\{\mathbf{u}\}$, where the braces $\{\}$ denote a *set* of \mathbf{u} in a simulation supercell, as

$$E^{\text{tot}} = V^{\text{self}}(\{\mathbf{u}\}) + V^{\text{dpl}}(\{\mathbf{u}\}) + V^{\text{short}}(\{\mathbf{u}\}) + V^{\text{elas}}(\eta_1, \dots, \eta_6) + V^{\text{int}}(\{\mathbf{u}\}, \eta_1, \dots, \eta_6). \quad (3)$$

Here V^{self} , V^{dpl} , V^{short} , V^{elas} , and V^{int} are a local-mode self-energy, a long-range dipole-dipole interaction, a short-range interaction between soft-modes, an elastic energy, and an interaction between the local modes and local strain, respectively. They employed Eq. (3) as an effective Hamiltonian for $\{\mathbf{u}\}$ in the supercell,

performed Monte-Carlo simulations, and demonstrated the ability to describe the phase transitions of bulk ferroelectrics. The coarse-graining that reduces the 15-dimensional atomic displacement vector v_α^r to a 3-dimensional local soft-mode amplitude vector u_α in each unit cell was shown to be a good approximation. However, the computation of V^{dpl} was still time-consuming, owing to the long-range Coulomb interaction, thus limiting system size and simulation time that could be handled in practical simulations.

In 2003, Waghmare, Cockayne, and Burton introduced a technique to decrease the computational time for V^{dpl} (or forces exerted on $\{\mathbf{u}\}$).¹³ Direct calculation of the forces in real space requires a computational time proportional to N^2 , i.e., $O(N^2)$, where N is the supercell size ($N = L_x \times L_y \times L_z$). It decreases to $O(N \log N)$ if one calculates the forces in reciprocal space using fast-Fourier transform (FFT) methods. This acceleration in computational speed enabled us to perform MD simulations on $\{\mathbf{u}\}$ in a large supercell, and was applied to bulk relaxor ferroelectrics.^{13,14}

Here, we explain how the fast MD method for simulating a first-principles effective Hamiltonian can be applied to study ferroelectric thin-film capacitor structures with short-circuited electrodes or external electric fields. This new MD method can simulate perovskite-type ferroelectric thin-film capacitors with dead layers and consequent depolarization fields. The high speed of this MD method enables us to simulate a ferroelectric material for a realistic system size (up to 100 nm) and a realistic time span (> 1 ns).

In the next section, we explain the formalism of the new MD-simulation method for thin-film capacitors. Results of simulations of BaTiO₃ bulk and thin-film capacitors are shown in Sec. III. In subsection III A, we confirm the reliability of our MD program by simulating thermal properties of bulk BaTiO₃. The advantage of this MD method compared to the Monte-Carlo method is also discussed. In subsection III B, we perform heating-up and cooling-down simulations for thin-film BaTiO₃ capacitors with perfect and imperfect electrodes. Thickness dependence of simulated striped domain structures in thin-film capacitors with imperfect electrodes are analyzed in detail. We have already reported some simulated results of thin-film capacitors of this subsection and determined thermal properties in Ref. [15] briefly. In subsection III C, newly obtained simulated results of hysteresis loops of thin-film capacitors are reported. In Sec. IV, we summarize the paper.

We named our MD program `feram` and distribute it as free software through <http://loto.sourceforge.net/feram/>.

II. FORMALISM AND METHOD OF CALCULATION

A. Effective Hamiltonian

The effective Hamiltonian used in the present MD simulations is basically the same as that in Ref. [13]. Here, we present the Hamiltonian with a notation similar to that in Ref. [11] as

$$\begin{aligned}
 H^{\text{eff}} = & \frac{M_{\text{dipole}}^*}{2} \sum_{\mathbf{R}, \alpha} \dot{u}_\alpha^2(\mathbf{R}) + \frac{M_{\text{acoustic}}^*}{2} \sum_{\mathbf{R}, \alpha} \dot{w}_\alpha^2(\mathbf{R}) \\
 & + V^{\text{self}}(\{\mathbf{u}\}) + V^{\text{dpl}}(\{\mathbf{u}\}) + V^{\text{short}}(\{\mathbf{u}\}) \\
 & + V^{\text{elas, homo}}(\eta_1, \dots, \eta_6) + V^{\text{elas, inho}}(\{\mathbf{w}\}) \\
 & + V^{\text{coup, homo}}(\{\mathbf{u}\}, \eta_1, \dots, \eta_6) + V^{\text{coup, inho}}(\{\mathbf{u}\}, \{\mathbf{w}\}) \\
 & - Z^* \sum_{\mathbf{R}} \boldsymbol{\mathcal{E}} \cdot \mathbf{u}(\mathbf{R}), \quad (4)
 \end{aligned}$$

where $\mathbf{u} = \mathbf{u}(\mathbf{R})$ and $\mathbf{w} = \mathbf{w}(\mathbf{R})$ are, respectively, the local soft-mode amplitude vector and the local acoustic displacement vector of the unit cell at \mathbf{R} , the α component of \mathbf{R} runs over

$$R_\alpha = 0, a_0, 2a_0, \dots, (L_\alpha - 1)a_0, \quad (5)$$

η_1, \dots, η_6 are the homogeneous strain components, and M_{dipole}^* and M_{acoustic}^* are the effective masses for \mathbf{u} and \mathbf{w} , respectively. Note that \mathbf{u} can also be considered as the optical displacement, in contrast to the acoustic displacement \mathbf{w} , or the dipole moment $Z^*\mathbf{u}$, where Z^* is the Born effective charge associated with the soft mode. In the effective Hamiltonian (4), external electric field $\boldsymbol{\mathcal{E}}$ is taken into account through its vector product with each dipole moment $Z^*\mathbf{u}$.

To determine the effective mass M_{dipole}^* , let $\epsilon_\alpha^\tau(\mathbf{k}, i)$ be a mass-weighted i -th eigenvector of the *phonon* dynamical matrix at wavevector \mathbf{k} . Its eigenvalue $\{\omega(\mathbf{k}, i)\}^2$ is the corresponding phonon frequency. Moreover, let $d_\alpha^\tau(\mathbf{k}, i) = \epsilon_\alpha^\tau(\mathbf{k}, i)/\sqrt{M^\tau}$ be an atomic displacement vector, which is normalized as $\sum_{\alpha, \tau} \{d_\alpha^\tau(\mathbf{k}, i)\}^2 = 1$ by adjusting the norm of $\boldsymbol{\epsilon}(\mathbf{k}, i)$. Here, M^τ is the mass of atom τ . Generally, the effective mass of a phonon is \mathbf{k} - and mode-dependent:

$$M^*(\mathbf{k}, i) = \sum_{\alpha, \tau} \{d_\alpha^\tau(\mathbf{k}, i)\}^2 M^\tau. \quad (6)$$

However, as an approximation, we have to employ a unique effective mass for dipoles in the MD simulation. Thus using the *steepest descent* Γ_{15} soft-mode normalized direction vectors $\boldsymbol{\xi}_z = (0.20, 0.76, -0.21, -0.21, -0.53)$ and $\boldsymbol{\xi}_x = \boldsymbol{\xi}_y = 0$ from Ref. [11], for BaTiO₃, we set M_{dipole}^* as

$$M_{\text{dipole}}^* = \sum_{\tau} \{\xi_z^\tau\}^2 M^\tau = 39.0 \text{ amu}. \quad (7)$$

It should be mentioned that ξ_z^τ is *not* equal to the d_α^τ of the Γ_{15} soft-mode of phonon, because M^A , M^B , and M^O are not identical.

The local-mode self-energy $V^{\text{self}}(\{\mathbf{u}\})$ is

$$V^{\text{self}}(\{\mathbf{u}\}) = \sum_{i=1}^N \left\{ \kappa_2 u^2(\mathbf{R}_i) + \alpha u^4(\mathbf{R}_i) + \gamma [u_y^2(\mathbf{R}_i) u_z^2(\mathbf{R}_i) + u_z^2(\mathbf{R}_i) u_x^2(\mathbf{R}_i) + u_x^2(\mathbf{R}_i) u_y^2(\mathbf{R}_i)] \right\}, \quad (8)$$

where $u^2(\mathbf{R}_i) = u_x^2(\mathbf{R}_i) + u_y^2(\mathbf{R}_i) + u_z^2(\mathbf{R}_i)$.

The long-range dipole-dipole interaction $V^{\text{dpl}}(\{\mathbf{u}\})$ is

$$V^{\text{dpl}}(\{\mathbf{u}\}) = \frac{1}{2} \sum_{i=1}^N \sum_{\alpha} \sum_{j=1}^N \sum_{\beta} u_{\alpha}(\mathbf{R}_i) \Phi_{\alpha\beta}(\mathbf{R}_{ij}) u_{\beta}(\mathbf{R}_j), \quad (9)$$

where

$$\Phi_{\alpha\beta}(\mathbf{R}_{ij}) = \frac{Z^{*2}}{\epsilon_{\infty}} \sum_{\mathbf{n}} \frac{\delta_{\alpha\beta} - 3(\widehat{\mathbf{R}_{ij} + \mathbf{n}})_{\alpha}(\widehat{\mathbf{R}_{ij} + \mathbf{n}})_{\beta}}{|\mathbf{R}_{ij} + \mathbf{n}|^3}, \quad (10)$$

ϵ_{∞} is the optical dielectric constant (or refractive index squared), $\delta_{\alpha\beta}$ is the Kronecker delta, a hat indicates a unit vector, \mathbf{n} is the supercell lattice vector

$$n_{\alpha} = \dots, -2L_{\alpha}a_0, -L_{\alpha}a_0, 0, L_{\alpha}a_0, 2L_{\alpha}a_0, \dots, \quad (11)$$

and a_0 is the equilibrium lattice constant. In Eq. (10), \sum' indicates that the summation does not include terms for which $\mathbf{R}_{ij} = \mathbf{n} = 0$.

We take account of short-range interactions between the optical displacements $\mathbf{u}(\mathbf{R})$ up to third nearest neighbor (3nn) as

$$V^{\text{short}}(\{\mathbf{u}\}) = \frac{1}{2} \sum_{i=1}^N \sum_{\alpha} \sum_{j=1}^{3\text{nn}} \sum_{\beta} u_{\alpha}(\mathbf{R}_i) J_{ij,\alpha\beta} u_{\beta}(\mathbf{R}_j), \quad (12)$$

where $J_{ij,\alpha\beta}$ is the short-range interaction matrix, which can be classified into 7 independent interaction parameters,¹¹ $J_{ij,\alpha\beta} = \pm j_k$ ($k = 1, \dots, 7$).

In practice, $\kappa_2 u_i^2$ in Eq. (8), Eq. (9), and Eq. (12), in which u_{α} is quadratic, are gathered and calculated in reciprocal space as

$$V^{\text{quad}}(\{\mathbf{u}\}) = \frac{1}{2} \sum_{\mathbf{k}} \sum_{\alpha,\beta} \tilde{u}_{\alpha}^*(\mathbf{k}) \tilde{\Phi}_{\alpha\beta}^{\text{quad}}(\mathbf{k}) \tilde{u}_{\beta}(\mathbf{k}), \quad (13)$$

where $\tilde{u}_{\alpha}(\mathbf{k})$ is the Fourier transform

$$\tilde{u}_{\alpha}(\mathbf{k}) = \sum_{\mathbf{R}} u_{\alpha}(\mathbf{R}) \exp(-i\mathbf{k} \cdot \mathbf{R}), \quad (14)$$

of $u_{\alpha}(\mathbf{R})$, $\tilde{\Phi}_{\alpha\beta}^{\text{quad}}(\mathbf{k})$ is similarly the Fourier transform of the quadratic interaction matrix (which is only calculated

once at the beginning of simulation),¹³ and \mathbf{k} is a reciprocal vector in the first Brillouin zone of the unit cell such as

$$k_{\alpha} = -\frac{L_{\alpha} - 1}{2L_{\alpha}} \frac{2\pi}{a_0}, \dots, -\frac{1}{L_{\alpha}} \frac{2\pi}{a_0}, 0, \frac{1}{L_{\alpha}} \frac{2\pi}{a_0}, \dots, \frac{1}{2} \frac{2\pi}{a_0}. \quad (15)$$

The homogeneous elastic energy $V^{\text{elas,homo}}(\eta_1, \dots, \eta_6)$ is

$$V^{\text{elas,homo}}(\eta_1, \dots, \eta_6) = \frac{N}{2} B_{11}(\eta_1^2 + \eta_2^2 + \eta_3^2) + N B_{12}(\eta_2\eta_3 + \eta_3\eta_1 + \eta_1\eta_2) + \frac{N}{2} B_{44}(\eta_4^2 + \eta_5^2 + \eta_6^2), \quad (16)$$

where B_{11} , B_{12} , and B_{44} are the elastic constants expressed in energy unit ($B_{11} = a_0^3 C_{11}$, $B_{12} = a_0^3 C_{12}$, and $B_{44} = a_0^3 C_{44}$).

The inhomogeneous elastic energy $V^{\text{elas,inho}}(\{\mathbf{w}\})$ is also calculated in reciprocal space as

$$V^{\text{elas,inho}}(\{\mathbf{w}\}) = \frac{1}{2} \sum_{\mathbf{k}} \sum_{\alpha,\beta} \tilde{w}_{\alpha}^*(\mathbf{k}) \tilde{\Phi}_{\alpha\beta}^{\text{elas,inho}}(\mathbf{k}) \tilde{w}_{\beta}(\mathbf{k}). \quad (17)$$

For the *force constant* matrix $\tilde{\Phi}_{\alpha\beta}^{\text{elas,inho}}(\mathbf{k})$, we employed the long-wavelength approximation. For instance, the diagonal part is

$$\tilde{\Phi}_{xx}^{\text{elas,inho}}(\mathbf{k}) = \frac{1}{N} [k_x^2 B_{11} + k_y^2 B_{44} + k_z^2 B_{44}], \quad (18)$$

and the off-diagonal part is

$$\tilde{\Phi}_{xy}^{\text{elas,inho}}(\mathbf{k}) = \frac{1}{N} [k_x k_y B_{12} + k_x k_y B_{44}]. \quad (19)$$

The coupling between $\{\mathbf{u}\}$ and homogeneous strain is the same as that given in Ref. [9], i.e.,

$$V^{\text{coup,homo}}(\{\mathbf{u}\}, \eta_1, \dots, \eta_6) = \frac{1}{2} \sum_{\mathbf{R}} \sum_{i=1}^6 \sum_{j=1}^6 \eta_i C_{ij} y_j(\mathbf{R}). \quad (20)$$

Here, $y_1(\mathbf{R}) = u_x^2(\mathbf{R})$, $y_2(\mathbf{R}) = u_y^2(\mathbf{R})$, $y_3(\mathbf{R}) = u_z^2(\mathbf{R})$, $y_4(\mathbf{R}) = u_y(\mathbf{R})u_z(\mathbf{R})$, $y_5(\mathbf{R}) = u_z(\mathbf{R})u_x(\mathbf{R})$, and $y_6(\mathbf{R}) = u_x(\mathbf{R})u_y(\mathbf{R})$,

$$\mathbf{C} = \begin{pmatrix} B_{1xx} & B_{1yy} & B_{1yy} & 0 & 0 & 0 \\ B_{1yy} & B_{1xx} & B_{1yy} & 0 & 0 & 0 \\ B_{1yy} & B_{1yy} & B_{1xx} & 0 & 0 & 0 \\ 0 & 0 & 0 & 2B_{4yz} & 0 & 0 \\ 0 & 0 & 0 & 0 & 2B_{4yz} & 0 \\ 0 & 0 & 0 & 0 & 0 & 2B_{4yz} \end{pmatrix}, \quad (21)$$

and B_{1xx} , B_{1yy} , and B_{4yz} are the coupling coefficients defined in Ref. [9].

The coupling between $\{\mathbf{u}\}$ and inhomogeneous strain is also calculated in reciprocal space as

$$V^{\text{coup,inho}}(\{\mathbf{u}\}, \{\mathbf{w}\}) = \frac{1}{2} \sum_{\mathbf{k}} \sum_{\alpha} \sum_{i=1}^6 \tilde{w}_{\alpha}(\mathbf{k}) \tilde{B}_{\alpha i}(\mathbf{k}) \tilde{y}_i(\mathbf{k}), \quad (22)$$

where $\tilde{w}_\alpha(\mathbf{k})$ and $\tilde{y}_i(\mathbf{k})$ are the Fourier transforms of $w_\alpha(\mathbf{R})$ and $y_i(\mathbf{R})$, respectively. For the 3×6 coupling

matrix $\mathbf{B}(\mathbf{k})$, we again employed the long-wavelength approximation

$$\tilde{\mathbf{B}}(\mathbf{k}) = \frac{1}{N} \begin{pmatrix} k_x B_{1xx} & k_x B_{1yy} & k_x B_{1yy} & 0 & 2k_z B_{4yz} & 2k_y B_{4yz} \\ k_y B_{1yy} & k_y B_{1xx} & k_y B_{1yy} & 2k_z B_{4yz} & 0 & 2k_x B_{4yz} \\ k_z B_{1yy} & k_z B_{1yy} & k_z B_{1xx} & 2k_y B_{4yz} & 2k_x B_{4yz} & 0 \end{pmatrix}. \quad (23)$$

In the present MD simulations of BaTiO₃, the parameters from Refs. [10] and [11], which are determined by first-principles calculations, are employed. As mentioned in Refs. [10] and [11], this parameter set leads to an underestimation of the Curie temperature T_C . To correct this underestimation, we follow these references in applying a negative pressure of $p = -5.0$ GPa in all simulations.

B. Molecular Dynamics

MD simulations with the effective Hamiltonian of Eq. (4) are performed in the canonical ensemble using the Nosé-Poincaré thermostat.¹⁶ This symplectic thermostat is so efficient that we can set the time step to $\Delta t = 2$ fs. In our present simulations, we thermalize the system for 40,000 time steps, after which we average the properties for 10,000 time steps.

In Fig. 1 we roughly illustrate how to calculate the forces exerted on $u_\alpha(\mathbf{R})$ with $\tilde{\Phi}_{\alpha\beta}^{\text{quad}}(\mathbf{k})$ in Eq. (13) and how the time evolution is simulated. First, $u_\alpha(\mathbf{R})$ is FFTed to $\tilde{u}_\alpha(\mathbf{k})$, the force $\tilde{F}_\alpha(\mathbf{k}) = -\sum_\beta \tilde{\Phi}_{\alpha\beta}^{\text{quad}}(\mathbf{k}) \tilde{u}_\beta(\mathbf{k})$ is calculated in reciprocal space, and then the force in real space is obtained by the inverse FFT of $\tilde{F}_\alpha(\mathbf{k})$. In practice, updates of $u_\alpha(\mathbf{R})$ and $\dot{u}_\alpha(\mathbf{R}) = \frac{\partial}{\partial t} u_\alpha(\mathbf{R})$ are processed in the manner of the Nosé-Poincaré thermostat.

The homogeneous strain components η_1, \dots, η_6 are determined by solving

$$\frac{\partial}{\partial \eta_i} \left[V^{\text{elas, homo}}(\eta_1, \dots, \eta_6) + V^{\text{coup, homo}}(\{\mathbf{u}\}, \eta_1, \dots, \eta_6) \right] = 0 \quad (24)$$

at each time step according to $\{\mathbf{u}\}$ so that η_1, \dots, η_6 minimize $V^{\text{elas, homo}}(\eta_1, \dots, \eta_6) + V^{\text{coup, homo}}(\{\mathbf{u}\}, \eta_1, \dots, \eta_6)$. While the local acoustic displacement $w_\alpha(\mathbf{R})$ could be treated as dynamical variables using the effective mass M_{acoustic}^* , we have instead chosen to integrate out these variables in a manner similar to the treatment of the homogeneous strain. That is, $w_\alpha(\mathbf{R})$ is determined so that $V^{\text{elas, inho}}(\{\mathbf{w}\}) + V^{\text{coup, inho}}(\{\mathbf{u}\}, \{\mathbf{w}\})$ becomes minimum at each time step according to $u_\alpha(\mathbf{R})$. Technically, the minimization is performed by solving the linear

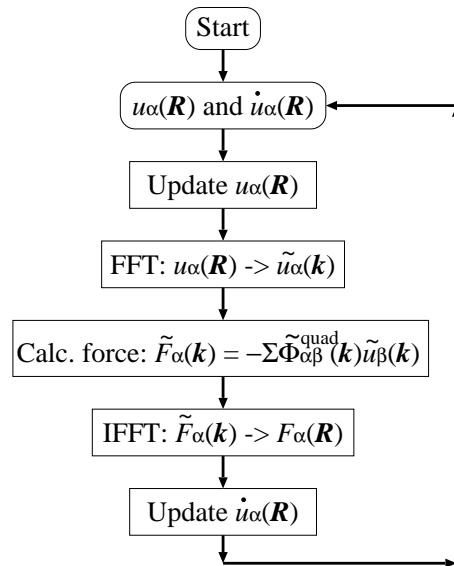


FIG. 1: Simplified flow chart for calculating forces on $u_\alpha(\mathbf{R})$. Fast Fourier transform (FFT) and inverse FFT (IFFT) enable rapid calculation of long-range dipole-dipole interactions.

set of equations

$$\tilde{\Phi}^{\text{elas, inho}}(\mathbf{k}) \tilde{\mathbf{w}}(\mathbf{k}) + \tilde{\mathbf{B}}(\mathbf{k}) \tilde{\mathbf{y}}(\mathbf{k}) = \mathbf{0} \quad (25)$$

for each \mathbf{k} in reciprocal space.

C. Ferroelectric Thin Films

If a ferroelectric thin film is placed in isolation in vacuum without electrodes as depicted in Fig. 2(a), its spontaneous polarization $\mathbf{P} = (P_x, P_y, P_z)$, which is represented by a thick arrow in the figure, induces charges $\pm\sigma_{\text{ind}} = \pm P_z$ at both surfaces, and the induced charges cause a full depolarization field in the thin film, $\mathcal{E}_d = -4\pi\sigma_{\text{ind}}\hat{z} = -4\pi P_z\hat{z}$. On the other hand, if the ferroelectric thin film is placed between short-circuited perfect electrodes as depicted in Fig. 2(b), the induced charges are fully canceled by free charges σ_{free} arising at both surfaces of the electrodes, $\mathcal{E}_d = -4\pi(\sigma_{\text{ind}} + \sigma_{\text{free}})\hat{z} = 0$. This geometric circumstance can be simulated with the doubly periodic supercell as depicted in Fig. 2(c), because

the two electrodes act as two electrostatic mirrors facing each other, and the mirrors make oppositely charged infinite mirror images beyond the electrodes.

We can also introduce dead layers of thickness d between the ferroelectric thin film and electrodes by constraining the local soft-mode amplitudes to vanish ($\mathbf{u} = 0$) in these layers, as illustrated in Fig. 2(d). With the dead layers, the infinite mirror images beyond the electrodes become $\frac{l}{l+d}$ more sparse than images of the without-dead-layer configuration. Consequently, the free charges arising at the electrode surfaces decrease to $\sigma_{\text{free}} = -\frac{l}{l+d}\sigma_{\text{ind}}$, where l is the ferroelectric film thickness. This simulates short-circuited imperfect electrodes resulting in a depolarization field of

$$\mathcal{E}_d = -4\pi \frac{d}{l+d} P_z \hat{\mathbf{z}}. \quad (26)$$

We can also use a doubly periodic supercell with dead layers for this case. Physically, the depolarization field of Eq. (26) can arise either from the presence of a dead layer in the ferroelectric near the interface, or from imperfect screening at the metal electrode, or both. We can define an effective screening length for each of these effects, and we interpret the “dead-layer thickness” d of our model as corresponding to the *sum* of these two physical screening lengths. The screening length associated with the electrode interface appears in Eq. (16) of Ref. [7] and Eq. (1) of Ref. [8] and is discussed for the SrRuO₃/BaTiO₃ interface in Refs. [17], [18], and [19]. Therefore, while the model does not explicitly incorporate information about the interface screening, this information is effectively included in the definition of the total screening length d in our model. Thus, for example, simulations at constant d for various film thicknesses can give the thickness dependence of the properties of capacitors with a certain interface structure.

In the present MD simulations, the local soft-mode amplitude vectors \mathbf{u} in dead layers are fixed to zero by the infinitely large mass. This infinitely-large-mass trick is congenial to the Nosé-Poincaré thermostat for maintaining the Nosé-Poincaré Hamiltonian at zero. Moreover, this treatment also has another advantage in that the short-range interactions between the surfaces of ferroelectric thin film and the electrodes are automatically truncated.

The depolarization field \mathcal{E}_d increases the total energy of the ferroelectric thin film by $-\mathbf{P} \cdot \mathcal{E}_d = 4\pi \frac{d}{l+d} P_z^2$. To avoid forming a depolarization field in ferroelectric thin films, it is known that the films often develop striped domain structures.^{20,21,22,23} The introduction of the striped domain structure can eliminate some part of the energy increase $4\pi \frac{d}{l+d} P_z^2$, because P_z becomes zero on average. However, the striped domain structure involves an energy cost in the short-range interaction $V^{\text{short}}(\{\mathbf{u}\})$, because it has domain boundaries between which \mathbf{u} has opposite direction $\pm z$. The shorter the wavelength λ of the striped domain structure, the weaker the depolarization field, but the higher the short-range interaction energy. The

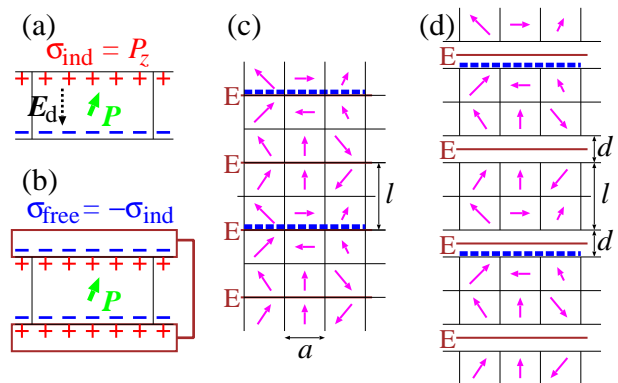


FIG. 2: Schematic illustrations of ferroelectric thin films of thickness l unit cells (here $l = 2$). (a) Isolated thin film in vacuum. (b) Thin film sandwiched between short-circuited perfect electrodes. Doubly periodic boundary conditions for simulations of films sandwiched between perfect and imperfect short-circuited electrodes are depicted in (c) and (d), respectively. Horizontal thick lines marked with “E” represent the electrostatic mirrors used to model electrodes. They are a distance $d/2$ away from the ferroelectric film surface ($d = 0$ in (c), $d = 1$ in (d)). Each thin arrow represents a local dipole within a unit cell ($a^3 = 3.94 \text{ \AA}^3$) of the BaTiO₃ crystal. Thick dashed lines enclose the periodic cell used for simulations.

ground state of a ferroelectric thin film will be decided by a competition between the long-range dipole-dipole interactions which favor a short-period domain structure, and domain-wall energy that arises from the short-range interactions and favors a uniformly polarized structure or a longer-period striped structure. In some previous works,^{24,25,26} the imperfect screening was mimicked with a parameter. On the other hand, our method with doubly periodic boundary condition does not require any parameters, because the effect of imperfectness of electrodes is automatically and implicitly included in the long-range dipole-dipole interaction $V^{\text{dpl}}(\{\mathbf{u}\})$.

III. RESULTS AND DISCUSSION

A. Bulk BaTiO₃

We first check the reliability of our MD program by comparing results of our simulations for bulk BaTiO₃ with earlier work based on the same effective Hamiltonian.^{10,11} We used a system size of $L_x \times L_y \times L_z = 16 \times 16 \times 16$ and small temperature steps in heating-up (+5 K/step) and cooling-down (−5 K/step) simulations, with initial configuration generated randomly: $\langle u_\alpha \rangle = 0.07 \text{ \AA}$ and $\langle u_\alpha^2 \rangle - \langle u_\alpha \rangle^2 = (0.02 \text{ \AA})^2$. We have also checked that there was no dependence of results of these simulations on initial configurations. The temperature dependence of the homogeneous strain components (see Fig. 3), which are the secondary order parameters of ferroelectric phase transitions, exhibits the correct se-

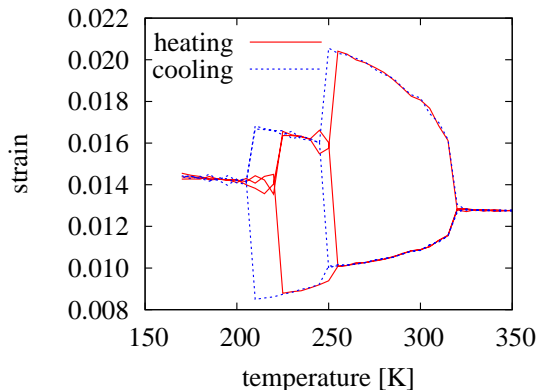


FIG. 3: Average homogeneous strains e_{xx} , e_{yy} , and e_{zz} as a function of temperature in heating-up (+5 K/simulation, solid lines) and cooling-down (-5 K/simulation, dashed lines) simulations for a $16 \times 16 \times 16$ supercell. Strains are measured relative to the LDA minimum-energy cubic structure with lattice constant 3.948 Å.

quence of phase transitions in BaTiO₃ known experimentally. Even under the negative pressure $p = -5.0$ GPa, the paraelectric to ferroelectric transition temperature T_C is underestimated at around 320 K in comparison with the experimental value of $T_C = 408$ K. Our estimates of T_C 's agree fairly well with the ones reported in Ref. [11]. The relatively weak first-order nature of the cubic-to-tetragonal phase transition in comparison with the first-order tetragonal-to-orthorhombic and orthorhombic-to-rhombohedral phase transitions is evident in the width of the temperature intervals of hysteresis (see Fig. 3). We note that the ability to simulate time-dependent phenomena is one of advantages of MD simulations compared to Monte-Carlo simulations.

B. BaTiO₃ ferroelectric thin-film capacitors

We now simulate and analyze the behavior of epitaxially grown films of BaTiO₃ on GdScO₃ substrates.² In our simulations, we represent this with 1% in-plane biaxial compressive strain by maintaining the homogeneous strain $\eta_1 = \eta_2 = -0.01$ and $\eta_6 = 0$. In other words, we maintained the average lattice constants a and b at $0.99a_0$ and angle γ at 90° . We use supercell sizes of $L_x \times L_y \times L_z = 32 \times 32 \times 2(l+d)$ and $40 \times 40 \times 2(l+d)$ and simulate ferroelectric layers of thickness l sandwiched between two short-circuited electrodes with ($d = 1$) and without ($d = 0$) dead layers. This is accomplished through use of doubly periodic boundary conditions as explained earlier.

Both the heating-up and cooling-down simulations are started with an initial configuration of $\langle u_x \rangle = \langle u_y \rangle = 0$, $\langle u_z \rangle = 0.07$ Å and $\langle u_\alpha^2 \rangle - \langle u_\alpha \rangle^2 = (0.02 \text{ Å})^2$. In the cooling-down simulations, which start at a sufficiently high temperature, the initial configuration changes to an

unpolarized one ($\langle u_z \rangle = 0$) during thermalization. We monitor the temperature dependence of $\langle u_\alpha \rangle$ and $\langle u_\alpha^2 \rangle$ for thin films with thicknesses $l = 15, 31, 127,$ and 255 with dead layers $d = 1$ and a thin film with thickness $l = 32$ without dead layers ($d = 0$) (see Fig. 4 and animations in the EPAPS²⁷). The behavior of the film with no dead layer is the same in heating and cooling simulations. In contrast, for the films with a dead layer ($d = 1$), the transition behavior exhibited by $\langle u_z \rangle = 0$ is rather different in heating and cooling simulations, although the temperature dependence of $\langle u_z^2 \rangle$ is almost the same in both the kinds of simulations. In the heating-up simulations, the discontinuity in $\langle u_z \rangle$ as a function of temperature marks a transition from a ferroelectric state with almost uniform out-of-plane polarization (Fig. 5(a)) to one with a striped domain structure (Fig. 5(b) and (c)). We find that this transition temperature, $T_S(l, d = 1)$, exhibits a strong dependence on size l . We note that this transition is missing in the cooling-down simulations; just above T_S , striped domain structures appear and the stripes remain and be frozen at $T < T_S$. The temperature $T_C(l, d = 1)$ at which $\sqrt{\langle u_z^2 \rangle}(T)$ exhibits a change in its slope marks another transition, namely from a striped domain phase to a paraelectric phase. $T_C(l, d = 1)$ depends relatively weakly on the film thickness. It should be mentioned that the results of heating-up simulations with a phase transition from the single domain state to the striped domain state at T_S below T_C agree with thermodynamical treatment of ferroelectric capacitors with dead layers by Chensky and Tarasenko.²⁸

For films with $d = 1$, T_S is 150 and 210 K for $l = 15$ and $l = 31$ respectively, which is lower than the bulk transition temperature ($T_C \approx 320$ K). However, for $d = 1$ films with $l = 127$ and $l = 255$, T_S is enhanced to 520 and 610 K respectively, well above the bulk T_C . In the infinite thickness limit ($l \rightarrow \infty$), it appears that $T_S(l, d = 1)$ tends to the T_C of thick films with no dead layer ($d = 0$), since T_C is 650 K for $l = 32$ and $d = 0$. In the $d = 1$ cases with $l = 127$ and $l = 255$, the effect arising from the depolarization field weakens significantly, and the enhancement of T_S results from the in-plane biaxial compressive strain. In the $d = 0$ case with $l = 32$, there is no depolarization field and enhancement of T_C by the in-plane biaxial compressive strain is effective even in very thin films. We note that $\sqrt{\langle u_z^2 \rangle}$ and $\sqrt{\langle u_x^2 \rangle}$ are distinct even at high temperatures (see Fig. 4e), indicating that the symmetry of the paraelectric phase is broken by the presence of the epitaxial constraint and the electrodes, as well as correlations between local dipoles and their images.

For films with a dead layer ($d = 1$), the striped domain structures appear in the cooling-down simulations at low temperatures for all values of thicknesses l explored here (see Fig. 5(b) and (c) for the case of $l = 15$ with $d = 1$, and Fig. 6 for various l). As shown in Table I, the wavevector \mathbf{k} of the striped domain, at which $\tilde{u}_z(\mathbf{k})$ has the largest amplitude $|\tilde{u}_z(\mathbf{k})|$, exhibits an interesting dependence on thickness l . We have determined \mathbf{k} for two

TABLE I: Dependence of the wavevector $\mathbf{k}/2\pi$ of the striped domain structure on thickness l in the thin-film BaTiO₃ capacitor with a dead layer ($d = 1$).

l	$32 \times 32 \times 2(l+d)$	$40 \times 40 \times 2(l+d)$
7	{ 4/32 3/32 0 }	{ 5/40 5/40 0 }
15	{ 3/32 3/32 0 }	{ 4/40 3/40 0 }
31	{ 2/32 2/32 0 }	{ 3/40 2/40 0 }
63	{ 2/32 1/32 0 }	{ 2/40 2/40 0 }
127	{ 1/32 1/32 0 }	{ 1/40 1/40 0 }
255	{ 1/32 0/32 0 }	{ 1/40 0/40 0 }

supercell sizes, $32 \times 32 \times 2(l+d)$ and $40 \times 40 \times 2(l+d)$, to identify supercell-size effects. It can be seen that, except for the data for $l = 255$, \mathbf{k} tends to be along the in-plane $\{110\}$ direction, consistent with earlier reports.^{25,29} The simulated striped domain structure for $l = 255$, which is parallel to the $\{100\}$ direction, is likely to be an artifact of the finite supercell-size: $L_x \times L_y = 32 \times 32$ or even 40×40 are too small to allow for the formation of a sufficiently thick $\{110\}$ striped domain. The wavelength $\lambda = 2\pi/|\mathbf{k}|$ of dominant periodicity of the domain pattern is shown as a function of thickness l in Fig. 7, where it is evident that the thinner films have smaller λ to avoid the stronger depolarization field, Eq. (26). The fitting shown in Fig. 7 suggests a square-root dependence²⁰ on l (the result for $l = 255$ is not included in the fit). Extensive simulations at larger length scales would probably be required to clarify further the dependence of the domain period of these striped structures on film thickness and dead-layer thickness.

The stark difference in the behavior of $\langle u_z \rangle$ in heating-up and cooling-down simulations hints that the (almost) uniformly polarized state and the $\langle u_z \rangle = 0$ striped domain states are frozen and thermal hopping between them may be almost impossible at low temperatures. To understand why both uniformly polarized and striped domain states are stable and thermal hopping between them are difficult, we investigated the effective potential-energy surfaces for striped domain structures of various stripe wavevectors \mathbf{k} and various l for thin-film ferroelectric capacitors with and without the dead layer (see Fig. 8(a)-(e)). Omitting surface relaxations in this analysis may be reasonable because the surface relaxations are confined to the surface region of the ferroelectric thin films as shown in Fig. 5(c). It can be seen that thinner ferroelectric film have a shorter stripe wavelength $\lambda = 2\pi/|\mathbf{k}|$ in their ground states. As the thickness l is increased to $l \approx 127$, the ground state changes from the striped domain structure to the out-of-plane uniformly-polarized ferroelectric structure ($\mathbf{k} = (000)$). However, on the time scale of our simulations (≈ 1 ns), even at $l \approx 255$ there is no hopping from the striped domain metastable state to the uniformly polarized ground state (Fig. 4(d)). It can also be seen in Fig. 8(a)-(e) that the magnitude of u_z which gives the minimum-energy ground state becomes larger, and the minimum energy gets

deeper, as l increases, in good correspondence with the thickness dependence of T_C . The trend of \mathbf{k} with l also shows good agreement with the simulated values shown in Table I. The simulated stability of the out-of-plane uniformly-polarized states against the energetically lower striped-domain states in thinner ($l < 127$) films at low temperature seems to give support to the recent idea of elastic stabilization of a homogeneously polarized state in strained ultrathin films.³⁰ As shown in Fig. 9(a), the polarization switching in the epitaxially constrained film may be suppressed by the presence of a potential barrier that prevents hopping between the uniformly-polarized and striped-domain states. For $l \leq 127$ with $d = 1$, it is expected that a uniformly polarized film would evolve into a striped domain state, or vice versa, over a sufficiently long time at $T < T_S$. However, the time scale of the evolution might be very much longer than the present simulation time scale (~ 1 ns). It might also be expected that, in the cooling-down simulations of films with $l \leq 127$ and $d = 1$, the uniformly polarized state is obtained at $T < T_S$. Instead, however, we find that stripes appear. A close inspection of the simulations shows that the stripes form slightly above T_S , initially in a somewhat disordered fashion, presumably because such a structure provides a good compromise between energetic and entropic considerations. The stripes then get frozen into place, and become better ordered, as the temperature is reduced below $T < T_S$. Conversely, in the case of $d = 0$ (Fig. 4(e), depolarization field $\mathcal{E}_d = 0$), the striped domain structure does not appear during the heating-up and cooling-down simulations. This may be because, when $\mathcal{E}_d = 0$, there is no reason or chance to form a striped domain structure even just above T_C . At T_C , direct phase transition from paraelectric phase to uniformly polarized ferroelectric phase occurs. Then, below T_C , the system tends to be in its ground state, the uniformly polarized ferroelectric structure.

C. Hysteresis loops

A measurement of polarization typically involves use of a triangle-wave electric field for recording the ferroelectric hysteresis loops (inset of Fig. 10). The hysteresis loops and coercive fields \mathcal{E}_c depend on the amplitude \mathcal{E}_0 and frequency f of the applied fields. We simulate hysteresis here using triangle-wave with steps (width $\Delta t n_{\text{steps}}$ and height $\Delta \mathcal{E}$) as sketched schematically in Fig. 10. Thus, the frequency of the applied field in our simulations is $f = \Delta \mathcal{E} / 4 \Delta t n_{\text{steps}} \mathcal{E}_0$. We used supercell sizes of $L_x \times L_y \times L_z = 16 \times 16 \times 2(l+d)$ in simulations of hysteresis loops for ferroelectric thin-film capacitors with 1% in-plane biaxial compressive strain and without constraints of strain (namely, the “free” film) (see Fig. 11). The temperature is maintained at 100 K through the simulations. For both the epitaxially constrained and “free” films, our simulations confirm that the imperfect screening of the electrodes decreases the coercive field as

the film thicknesses decreases, as described phenomenologically in Ref. [8]. There is a large (order-of-magnitude) difference in the coercive field \mathcal{E}_c between the epitaxially constrained film and the “free” film. This may be because the compressive strain arising from epitaxial constraints prevents the polarization switching, while the inclusion of inhomogeneous strain (i.e., acoustic displacements) eases the switching, as depicted in Fig. 9. The potential barriers themselves are lower in the “free” films than in the epitaxially constrained films (see Fig. 8). We note that hysteresis loops for “free” film capacitors with $l = 63$ and $l = 127$ are very similar to the experimentally observed hysteresis loops of a ferroelectric capacitor with damaged electrodes that have “steps” and “plateaus” during polarization switchings.¹ This is because, in the “free” film capacitors with imperfect electrodes ($d = 1$), the configuration with out-of-plane polarization is no longer the ground state. In fact, the ground state has a nonzero in-plane polarization. Thus, the dipoles $Z^* \mathbf{u}(\mathbf{R})$ have large in-plane components $Z^* u_x(\mathbf{R})$ and $Z^* u_y(\mathbf{R})$ in the hysteresis-loop simulations (and experiments), as evident in the snapshot shown in Fig. 12.

Unfortunately, attempts to fit our results to the usually-assumed Kay-Dunn scaling of the coercive field \mathcal{E}_c with film thickness l of thicker films³¹ were unsuccessful, as were attempts to emulate the relatively weak dependence of \mathcal{E}_c on l for epitaxially grown high-quality ultrathin films.^{32,33,34} The experimentally observed values of coercive fields \mathcal{E}_c for ultrathin BaTiO₃ capacitors range from 200 to 500 kV/cm,^{32,33,34} while simulations of epitaxially constrained films largely overestimate \mathcal{E}_c , and those of “free” films slightly underestimate \mathcal{E}_c . This may be because the switching in real thin-film capacitors is a large-scale (> 100 nm) phenomenon involving defect-mediated nucleation mainly at ferroelectrics-electrodes interfaces,^{18,31,35,36,37,38} as well as the possibility that the strain conditions may be intermediate between the cases of epitaxially constrained and “free” films. Such intermediate strain conditions may be achieved and will be simulated with MD in the future by introducing a mechanical boundary condition such as presented in Ref. [30]. In contrast to our case of ultrathin BaTiO₃ capacitors, it is well known that for ultrathin PbZr _{x} Ti _{$1-x$} O₃ (PZT) capacitors the coercive fields \mathcal{E}_c increase with decreasing film thickness l , and there is an

argument whether this strong increase of \mathcal{E}_c is coming from compressive substrate-induced lattice strain³⁹ or not.⁴⁰ Constructing a first-principles Hamiltonian for PZT and simulations with this MD method will help us to understand this difference between BaTiO₃ and PZT.

IV. SUMMARY

We have developed a robust and highly efficient molecular-dynamics scheme, based on a first-principles effective Hamiltonian formulation, for simulating the behavior of the polarization in perovskite-type ferroelectrics. We have applied this approach to study BaTiO₃ ferroelectric thin-film capacitors, with special attention to the dependence on film thickness and choice of electric boundary conditions. We find that striped domain structures tend to form on cooling-down simulations when a ferroelectric dead layer is present near the electrodes, and we study the dependence of the domain period on the conditions of formation. We also study the hysteresis loops for capacitor structures, both with and without such dead layers, and we find dramatic differences in the hysteretic behavior for the cases of elastically constrained or “free” films. Our MD simulator **feram** will be a powerful tool for further investigations of the physical properties of ferroelectric nanostructures that are relevant for a variety of potential device applications.

Acknowledgments

Computational resources were provided by the Center for Computational Materials Science, Institute for Materials Research (CCMS-IMR), Tohoku University. We thank the staff at CCMS-IMR for their constant effort. This research was done when T.N. stayed at JNCASR and Rutgers University under the support from JNCASR, Rutgers University, the Ministry of Education, Culture, Sports, Science and Technology (MEXT) of Japan, and the Japan Society for the Promotion of Science (JSPS). D.V. acknowledges support of ONR Grant N00014-05-1-0054.

¹ J. F. Scott, *Ferroelectric Memories* (Springer-Verlag, Berlin Heidelberg, 2000).

² K. J. Choi, M. Biegalski, Y. L. Li, A. Sharan, J. Schubert, R. Uecker, P. Reiche, Y. B. Chen, X. Q. Pan, V. Gopalan, et al., *Science* **306**, 1005 (2004).

³ M. E. Drougard and R. Landauer, *J. Appl. Phys.* **30**, 1663 (1959).

⁴ S. L. Miller, R. D. Nasby, J. R. Schwank, M. S. Rodgers, and P. V. Deessendorger, *J. Appl. Phys.* **68**, 6463 (1990).

⁵ V. V. Lemanov and V. K. Yarmarkin, *Phys. Solid State* **38**, 1363 (1996), [*Fiz. Tverd. Tela* **38**, 2482 (1996)].

⁶ H. Z. Jin and J. Zhu, *J. Appl. Phys.* **92**, 4594 (2002).

⁷ R. R. Mehta, B. D. Silverman, and J. T. Jacobs, *J. Appl. Phys.* **44**, 3379 (1973).

⁸ M. Dawber, P. Chandra, P. B. Littlewood, and J. F. Scott, *J. Phys.-Condens. Matter* **15**, L393 (2003).

⁹ R. D. King-Smith and D. Vanderbilt, *Phys. Rev. B* **49**, 5828 (1994).

- ¹⁰ W. Zhong, D. Vanderbilt, and K. M. Rabe, *Phys. Rev. Lett.* **73**, 1861 (1994).
- ¹¹ W. Zhong, D. Vanderbilt, and K. M. Rabe, *Phys. Rev. B* **52**, 6301 (1995).
- ¹² U. V. Waghmare and K. M. Rabe, *Phys. Rev. B* **55**, 6161 (1997).
- ¹³ U. V. Waghmare, E. J. Cockayne, and B. P. Burton, *Ferroelectrics* **291**, 187 (2003).
- ¹⁴ B. P. Burton, E. Cockayne, and U. V. Waghmare, *Phys. Rev. B* **72**, 064113 (2005).
- ¹⁵ J. Paul, T. Nishimatsu, Y. Kawazoe, and U. V. Waghmare, *Phys. Rev. Lett.* **99**, 077601 (2007).
- ¹⁶ S. D. Bond, B. J. Leimkuhler, and B. B. Laird, *J. Comput. Phys.* **151**, 114 (1999).
- ¹⁷ N. Sai, A. M. Kolpak, and A. M. Rappe, *Phys. Rev. B* **72**, 020101 (2005).
- ¹⁸ D. J. Kim, J. Y. Jo, Y. S. Kim, Y. J. Chang, J. S. Lee, J.-G. Yoon, T. K. Song, and T. W. Noh, *Phys. Rev. Lett.* **95**, 237602 (2005).
- ¹⁹ G. Gerra, A. K. Tagantsev, N. Setter, and K. Parlinski, *Phys. Rev. Lett.* **96**, 107603 (2006).
- ²⁰ C. Kittel, *Phys. Rev.* **70**, 965 (1946).
- ²¹ D. D. Fong, G. B. Stephenson, S. K. Streiffer, J. A. Eastman, O. Auciello, P. H. Fuoss, and C. Thompson, *Science* **304**, 1650 (2004).
- ²² A. M. Bratkovsky and A. P. Levanyuk, *Phys. Rev. Lett.* **84**, 3177 (2000).
- ²³ A. M. Bratkovsky and A. P. Levanyuk, *Phys. Rev. Lett.* **87**, 179703 (2001).
- ²⁴ B. K. Lai, I. Ponomareva, I. I. Naumov, I. Kornev, H. X. Fu, L. Bellaiche, and G. J. Salamo, *Phys. Rev. Lett.* **96**, 137602 (2006).
- ²⁵ B.-K. Lai, I. Ponomareva, I. A. Kornev, L. Bellaiche, and G. J. Salamo, *Phys. Rev. B* **75**, 085412 (2007).
- ²⁶ B.-K. Lai, I. Ponomareva, I. Kornev, L. Bellaiche, and G. Salamo, *Appl. Phys. Lett.* **91**, 152909 (2007).
- ²⁷ See EPAPS Document No. XXXXX for animations of the cooling-down and heating-up simulations. This document can be reached through a direct link in the online article's HTML reference section or via the EPAPS homepage <http://www.aip.org/pubservs/epaps.html>. Before PRB accept this manuscript, animations are temporally placed at <http://www-lab.imr.tohoku.ac.jp/%7Et-nissie/animations/>.
- ²⁸ E. V. Chensky and V. V. Tarasenko, *Sov. Phys. JETP* **56**, 618 (1982).
- ²⁹ S. Tinte and M. G. Stachiotti, *Phys. Rev. B* **64**, 235403 (2001).
- ³⁰ N. A. Pertsev and H. Kohlstedt, *Phys. Rev. Lett.* **98**, 257603 (2007).
- ³¹ H. F. Kay and J. W. Dunn, *Phil. Mag.* **7**, 2027 (1962).
- ³² Y. S. Kim, J. Y. Jo, D. J. Kim, Y. J. Chang, J. H. Lee, T. W. Noh, T. K. Song, J.-G. Yoon, J. S. Chung, S. I. Baik, et al., *Appl. Phys. Lett.* **88**, 072909 (2006).
- ³³ J. Y. Jo, Y. S. Kim, T. W. Noh, J.-G. Yoon, and T. K. Song, *Appl. Phys. Lett.* **89**, 232909 (2006).
- ³⁴ A. Petraru, N. A. Pertsev, H. Kohlstedt, U. Poppe, R. Waser, A. Solbach, and U. Klemradt, *J. Appl. Phys.* **101**, 114106 (2007).
- ³⁵ V. Janovec, *Czech. J. Phys.* **8**, 3 (1958).
- ³⁶ P. Chandra, M. Dawber, P. B. Littlewood, and J. F. Scott, *Ferroelectrics* **313**, 7 (2004).
- ³⁷ A. K. Tagantsev and G. Gerra, *J. Appl. Phys.* **100**, 051607 (2006).
- ³⁸ J. Y. Jo, D. J. Kim, Y. S. Kim, S.-B. Choe, T. K. Song, J.-G. Yoon, and T. W. Noh, *Phys. Rev. Lett.* **97**, 247602 (2006).
- ³⁹ N. A. Pertsev, J. R. Contreras, V. G. Kukhar, B. Hermanns, H. Kohlstedt, and R. Waser, *Appl. Phys. Lett.* **83**, 3356 (2003).
- ⁴⁰ H. N. Lee, S. M. Nakhmanson, M. F. Chisholm, H. M. Christen, K. M. Rabe, and D. Vanderbilt, *Phys. Rev. Lett.* **98**, 217602 (2007).

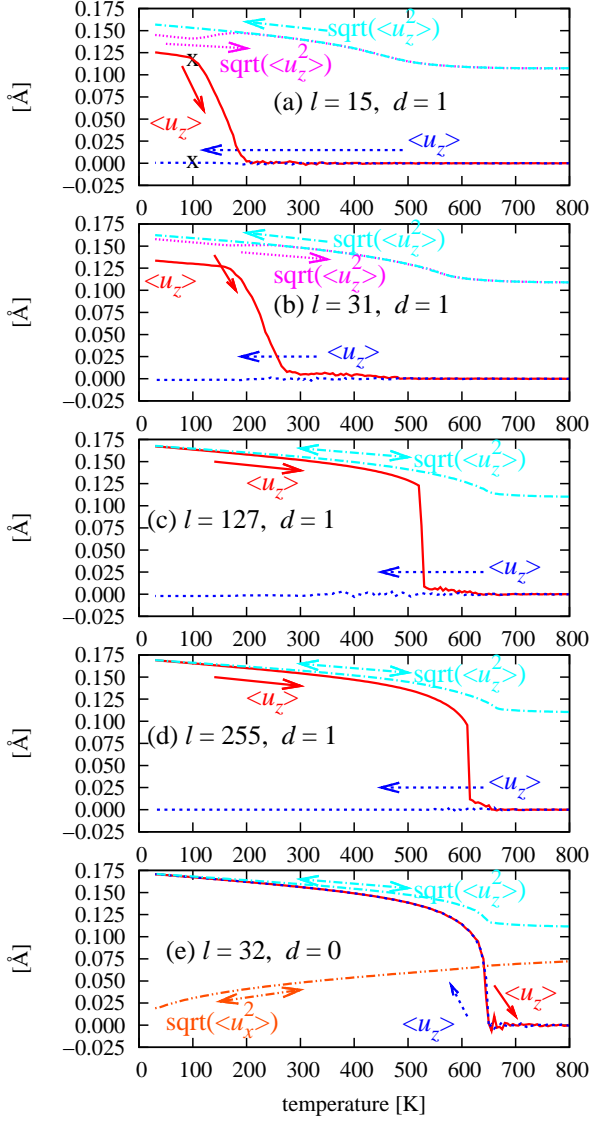


FIG. 4: $\langle u_z \rangle$ of heating-up (solid lines) and cooling-down (dashed lines) molecular-dynamics simulations of BaTiO₃ thin-film capacitors with short-circuited electrodes under 1% in-plane biaxial compressive strain for (a) thickness $l = 15$ layer with dead layer $d = 1$, (b) $l = 31$ with $d = 1$, (c) $l = 127$ with $d = 1$, (d) $l = 255$ with $d = 1$, and (e) $l = 32$ without dead layer ($d = 0$). $\sqrt{\langle u_z^2 \rangle}$ are also plotted in (a)-(e). In (c)-(e), heating-up $\sqrt{\langle u_z^2 \rangle}$ and cooling-down $\sqrt{\langle u_z^2 \rangle}$ are almost identical. $\sqrt{\langle u_x^2 \rangle}$ is plotted only in (e), because the behaviors of $\sqrt{\langle u_x^2 \rangle}$ and $\sqrt{\langle u_y^2 \rangle}$ are essentially identical in cases (a)-(e) (for both heating-up and cooling-down). Supercells are of size $32 \times 32 \times 2(l + d)$. Animations of these cooling-down and heating-up simulations are also available in the EPAPS.²⁷

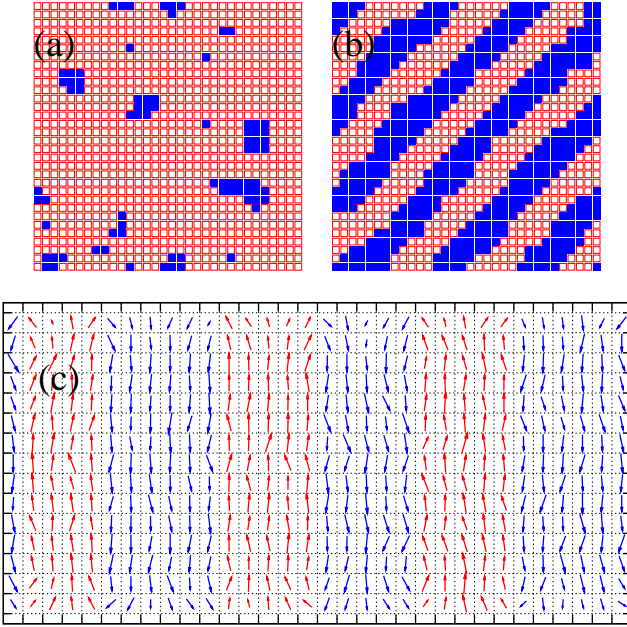


FIG. 5: Snapshots at $T = 100$ K in heating-up ((a)) and cooling-down ((b) and (c)) simulations of ferroelectric thin-film capacitors of $l = 15$ with $d = 1$. (a) and (b) are horizontal slices. (c) is a vertical cross section. Points of snapshots are indicated with “X” marks in Fig. 4(a). In horizontal slices, the $+z$ -polarized and $-z$ -polarized sites are denoted by \square and \blacksquare , respectively. In vertical cross sections, the dipole moments of each site are projected onto the xz -plane and indicated with arrows. Layers which do not have arrows are dead layers.

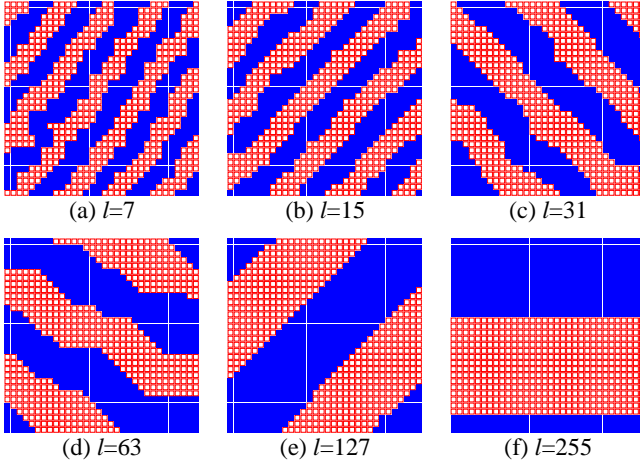


FIG. 6: Horizontal slices of snapshots at 100 K in cooling-down simulations of ferroelectric thin-film capacitors with single dead layer ($d = 1$) of various thickness $l = 7, 15, 31, 63, 127,$ and 255 . The $+z$ -polarized and $-z$ -polarized sites are denoted by \square and \blacksquare , respectively.

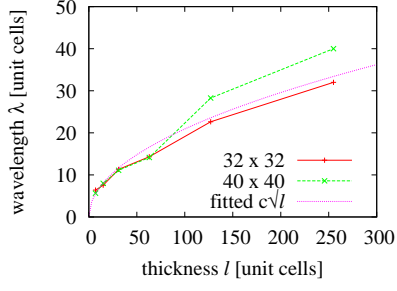


FIG. 7: Calculated thickness l dependence of wavelength λ of striped domain structures in thin film BaTiO_3 capacitors with a dead layer ($d = 1$). + marks are from $32 \times 32 \times 2(l+d)$ supercell calculations and \times are those of $40 \times 40 \times 2(l+d)$. Data of $l \leq 127$ are fitted with $\lambda = c\sqrt{l}$ (dotted line). $l = 255$ data are omitted, because of their large supercell-size dependence.

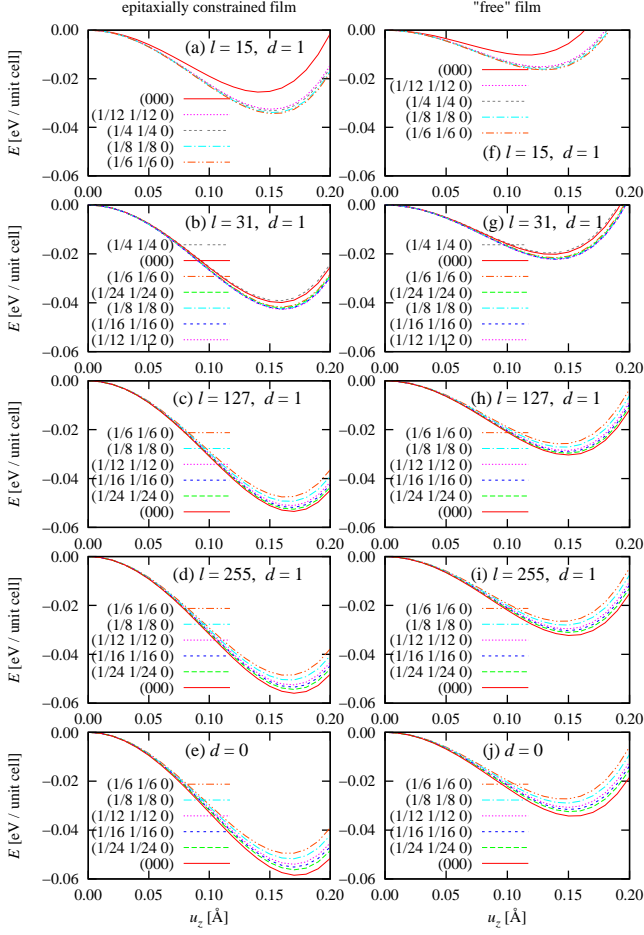


FIG. 8: Effective potential surfaces of BaTiO₃ thin-film capacitors with short-circuited electrodes: (a)-(e), under 1% in-plane biaxial compressive strain arising from epitaxial constraints; (f)-(j), without epitaxial constraints (i.e., for “free” films). The thicknesses of ferroelectric films and dead layers are indicated in each panel with l and d respectively. Total energies as functions of u_z are compared among striped domain structures with wavevectors \mathbf{k} parallel to (110). $\mathbf{k} = (000)$ corresponds to the uniformly polarized structure. The zero of the energy scale is placed at the total energy of the non-polarized $u_z = 0$ structure. A negative pressure $p = -5$ GPa is applied to correct the underestimation in T_C .

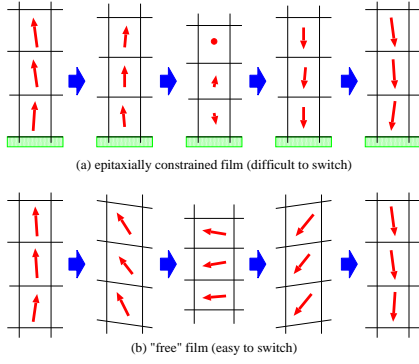


FIG. 9: Schematic comparison between the epitaxially constrained film and the “free” film. In the epitaxially constrained film, switching may have to climb over a potential barrier, but, in the “free” film, dipoles can be easily rotated and switching can go around a valley of the potential.

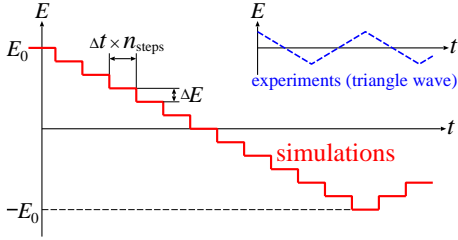


FIG. 10: Schematic illustrations of triangle-wave electric field used to measure ferroelectric hysteresis loops experimentally (inset) and in the present simulations.

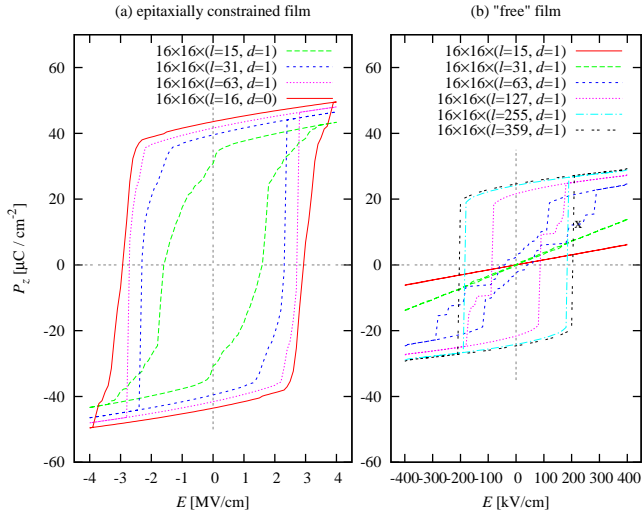


FIG. 11: Calculated hysteresis loops for capacitors with (a) epitaxially constrained films, and (b) “free” films of various thickness l and with dead layer d . Supercell sizes were $16 \times 16 \times 2(l+d)$. $\Delta t = 2$ fs and $n_{\text{steps}} = 50,000$. For epitaxially constrained films, $\mathcal{E}_0 = 4,000$ kV/cm and $\Delta \mathcal{E} = 100$ kV/cm are employed. For “free” films, $\mathcal{E}_0 = 400$ kV/cm and $\Delta \mathcal{E} = 10$ kV/cm are employed.

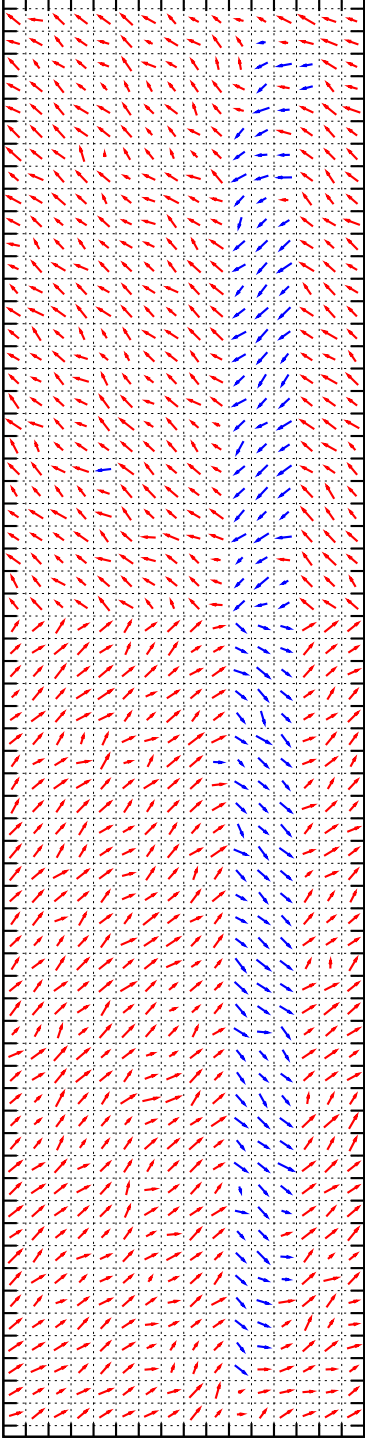


FIG. 12: Vertical cross section of a simulated ferroelectric “free” film capacitor with a single dead layer; $16 \times 16 \times (l = 63, d = 1)$. The snapshot was taken at the point marked “x” in Fig. 11(b). The projection of the dipole moments onto the xz -plane are indicated with arrows.